ICES Journal of Marine Science (2011), 68(6), 1030–1044. doi:10.1093/icesjms/fsr068

What ocean biogeochemical models can tell us about bottom-up control of ecosystem variability

A. Gnanadesikan*, J. P. Dunne, and J. John

NOAA Geophysical Fluid Dynamics Laboratory, Princeton University, 201 Forrestal Road, Princeton, NJ 08540, USA

**Corresponding Author: Current address: Department of Earth and Planetary Sciences, Johns Hopkins University, Baltimore, MD, USA; tel: +1 410 5160722; fax: +1 410 5167933; e-mail: gnanades@jhu.edu*

Gnanadesikan, A., Dunne, J. P., and John, J. 2011. What ocean biogeochemical models can tell us about bottom-up control of ecosystem variability. – ICES Journal of Marine Science, 68: 1030–1044.

Received 16 June 2010; accepted 20 March 2011

Processes included in earth system models amplify the impact of climate variability on phytoplankton biomass and, therefore, on upper trophic levels. Models predict much larger relative interannual variability in large phytoplankton biomass than in total phytoplankton biomass, supporting the goal of better constraining size-structured primary production and biomass from remote sensing. The largest modelled variability in annually averaged large phytoplankton biomass is associated with changes in the areal extent of relatively productive regions. Near the equator, changes in the areal extent of the high-productivity zone are driven by large-scale shifts in nutrient fields, as well as by changes in currents. Along the poleward edge of the Subtropical Gyres, changes in physical mixing dominate. Finally, models indicate that high-latitude interannual variability in large phytoplankton biomass is greatest during spring. Mechanisms for producing such variability differ across biomes with internal ocean processes, such as convection complicating efforts to link ecosystem variability to climate modes defined using sea surface temperature alone. In salinity-stratified subpolar regions, changes in bloom timing driven by salinity can produce correlations between low surface temperatures and high productivity, supporting the potential importance of using coupled atmosphere–ocean reanalyses, rather than simple forced ocean reanalyses, for attributing past ecosystem shifts.

Keywords: biome extent, climate models, nutrient limitation, salinity, size structure, spring bloom.

Introduction

As earth system models are developed for projecting biogeochemical changes under global warming, a natural question that arises is whether they will be useful for projecting changes in fisheries production, particularly those driven by bottom-up changes in the productivity or species composition associated with phytoplankton. One potential test is whether such models can simulate interannual variability. Variability in the stocks of a number of species has been reported on interannual to decadal scales and linked to climate modes, such as the Pacific Decadal Oscillation and North Atlantic Oscillation. For example, basin-scale modes in the Pacific have been linked to variability in species, such as salmon in the Pacific Northwest (Mantua *et al.*, 1997), walleye pollock in the Bering Sea (Hunt *et al.*, 2008), Japanese eel in the Kuroshio region (Sugimoto *et al.*, 2001; Kimura and Tsukamoto, 2006), and sardine and anchovy in the Peru Current (Chavez *et al.*, 2003).

Physical climate models might be able to address proposed mechanisms for interannual changes in stocks, such as temperature impacts on spawning times and locations (Genner *et al.*, 2004), changes in the frequency of warm events, such as those associated with coral bleaching (Glynn and de Weerdt, 1991), changes in the frequency of cold events associated with winter mortality (Hare *et al.*, 2010), or changes in the advective pathways for larval transport (Sugimoto *et al.*, 2001; Kimura and Tsukamoto, 2006). Although not deprecating the potential importance of such direct physical forcing for individual species, this paper focuses on simulations of primary productivity provided by a new generation of earth system models. For many years, fisheries oceanographers have recognized that the details of primary production, such as the timing of blooms (Hjort, 1914; Cushing, 1990) or differences in phytoplankton community structure (Ryther, 1969), could explain variations in ecosystems over time and space. We examine whether the large-scale earth system models used for projecting climate change represent these aspects of the primary productivity signal that both observations and theory suggest should vary significantly from year to year. Additionally, we investigate which models can tell us about the magnitude of such variability and about the physical processes underlying it. We demonstrate that the current generation of earth system models does simulate drivers of interannual ecosystem variability beyond annually averaged changes in biomass. These drivers include changes in the areal extent of productive regions, changes in the timing of blooms, and changes in the concentration of large phytoplankton.

Variability in the abundance of large phytoplankton is especially important, because grazing on these organisms has long been thought to represent the key pathway by which energy is transferred to higher trophic levels, resulting in the classic statement that "all fish is diatoms" (Bigelow, 1926). In upwelling

regions rich in macronutrients, larger phytoplankton dominate and recycling of nutrient is inefficient (Dugdale and Goering, 1967). In weakly productive Subtropical Gyres, where macronutrients are at low levels, small picoplankton have been recorded to account for most of the primary productivity (Platt *et al.*, 1983) and recycling of nutrients is high. This results in less variation in total biomass across biomes than would be expected from the differences in nutrient supply, as well as less spatial variability in small phytoplankton biomass than large phytoplankton biomass. Agawin *et al.* (2000) noted that large plankton biomass concentrations vary over 5–6 orders of magnitude in mesocosm experiments, whereas small plankton biomass concentrations vary over ~2 orders of magnitude. Kostadinov *et al.* (2009) found greater spatial variation in large particle concentrations than small particle concentrations, and Uitz *et al.* (2010) found greater temporal variability in remotely sensed primary productivity associated with large phytoplankton than that associated with small phytoplankton. The idea that such differences in the size structure of primary producers, translated up the foodweb, are responsible for differences in fisheries production between ecosystems goes back at least to Ryther (1969). However, because *in situ* time-series of size-fractionated productivity and biomass do not exist for most of the regions displaying large relative variability, it is worth examining whether models could be used to characterize the variability of large phytoplankton on global scales.

The current generation of ocean biogeochemical and earth system models combine information about physical forcing, chemical cycling, phytoplankton physiology, and ecological structure to simulate the response of lower trophic levels to climate variability and change (Six and Meier-Reimer, 1996; Moore *et al.*, 2002; Aita *et al.*, 2003, 2007; Aumont and Bopp, 2006; Galbraith *et al.*, 2010; Kishi *et al.*, 2010). Built around ocean circulation models that use the conservation of heat, mass, salt, and momentum to solve for a physical circulation consistent with surface forcing, such models can be forced by datasets based on atmospheric reanalysis products (Griffies *et al.*, 2009) to produce retrospective estimates of biological activity. Alternatively, they can be embedded in fully coupled ocean–atmosphere circulation models to estimate how ocean ecosystems might change in future because of changes in greenhouse gases (Steinacher *et al.*, 2010).

This paper examines which such models can tell us about the potential for linking variability in primary productivity quantitatively and mechanistically to climate variability and change. We first describe how the Tracers of Ocean Productivity with Allometric Zooplankton (TOPAZ) model (Dunne *et al.*, 2010) used in the National Oceanographic and Atmospheric Administration's (NOAA) Geophysical Fluid Dynamics Laboratory's (GFDL) Earth System Model 2.1 (ESM2.1) represents key ideas about phytoplankton size structure and describes two physical circulation models where it has been implemented. We then present output from these simulations, quantifying the dominance of large phytoplankton variability over much of the ocean, further highlighting the importance of changes in areal extent of biomes and considering the impact of interannual variability in bloom timing. Next, we expand on the mechanisms by which tropical variability on interannual time-scales changes the areal extent of the oligotrophic tropical gyres. We move on to address the mechanisms driving interannual variability in spring productivity in four North Pacific regions. We conclude the paper by examining the implications of our results on the characterization of fisheries observationally and for developing new retrospective modelling analyses.

The models

Size structure in the GFDL ecosystem models

We begin by describing the ecosystem model used in one ESM, GFDL's TOPAZ code. A preliminary description of the TOPAZ biogeochemical model is presented in Dunne *et al.* (2010). We therefore focus on how the model represents the response of phytoplankton biomass to varying environmental conditions and how this response differs between large and small phytoplankton.

Like other biogeochemical models of intermediate complexity, TOPAZ divides the phytoplankton community into a small number of functional groups that react differently to light and nutrient limitation. The growth rate of a given class of phytoplankton is given by

$$\mu = \frac{P^{C}_{max}}{1+\zeta} e^{kT} \min(\mathrm{Lim_N}, \mathrm{Lim_P}, \mathrm{Lim_{Fe}}) \times \mathrm{Lim_{Irr}}, \quad (1)$$

where P^{C}_{max} is a maximum carbon assimilation rate (s^{-1}), ζ the cost of biosynthesis (set to 0.1), k the Eppley temperature coefficient (0.063 K^{-1}), T the temperature (K), and $\mathrm{Lim_{N,P,Fe,Irr}}$ refer to the limitation terms for nitrogen, phosphorus, iron, and light, respectively. Phytoplankton are then limited by the temperature, whatever nutrient is most limiting, and by light. Nitrogen limitation is given by

$$\mathrm{Lim_N} = \max\left(\frac{\mathrm{NO_3}}{K_{\mathrm{NO_3}} + \mathrm{NO_3}(1 + \mathrm{NH_4}/K_{\mathrm{NH_4}})}, \frac{\mathrm{NH_4}}{K_{\mathrm{NH_4}} + \mathrm{NH_4}}\right), \quad (2)$$

following Frost and Franzen (1992), with NO_3 and NH_4 referring to the ambient nitrate concentrations, so that nitrate limitation becomes less important in the presence of ammonia. The physiological nutrient limitation terms $\mathrm{Lim_{P,Fe}}$ are determined from the actual N:P and Fe:P cellular quotas, which change through a complicated process described in detail in Dunne *et al.* (2010), based on the theoretical work of Klausmeier *et al.* (2004). Because these terms turn out to be of minor importance in the regions presented below, Dunne *et al.* (2010) should be consulted for a complete description of how they work; this will not be discussed further here.

Light limitation is parametrized as

$$\mathrm{Lim_{Irr}} = 1 - \exp\left(-\alpha\theta\frac{I}{P^{C}_{N}}\right). \quad (3)$$

In this equation, α is the initial slope of the chlorophyll a (Chl) specific photosynthesis–light response curve [units of mol C (mol Chl J m^{-2})$^{-1}$]; therefore, it governs how rapidly photosynthesis (relative to chlorophyll) increases at low light levels assuming constant chlorophyll. θ is the chlorophyll to carbon ratio [Chl : C; mol Chl (mol C)$^{-1}$], I the incoming solar radiation in (W m^{-2}), and $P^{C}_{N} = P^{C}_{max} e^{kT} \min(\mathrm{Lim_N}, \mathrm{Lim_P}, \mathrm{Lim_{Fe}})$ the nutrient-limited carbon assimilation rate (s^{-1}). In a modified version of the formulation proposed by Geider *et al.* (1997), we then let

$$\theta = \theta_{min} \min(\mathrm{Lim_N}, \mathrm{Lim_P}, \mathrm{Lim_{Fe}}) + \frac{\theta_{max} - \theta_{min}}{1 + \alpha(\theta_{max} - \theta_{min})I/2P^{C}_{N}}, \quad (4)$$

so that as nutrients increase (or light decreases), the Chl:C level ratio increases to match the increased need for light-harvesting efficiency. This means that variations in chlorophyll concentration can be driven by variations in the available light (e.g. because of changing insolation or mixed-layer depth), which will not necessarily reflect changes in biomass. In contrast to the version of the code used in Sarmiento *et al.* (2010), we do not let θ_{max} depend on iron limitation. As discussed in Galbraith *et al.* (2010), the primary impact of neglecting such dependence is seen in the North Atlantic, where high levels of iron allow an earlier spring bloom and faster drawdown of surface nutrients.

The concentration of phytoplankton is determined by a balance between the growth rate and the grazing rate. The representation of grazing in TOPAZ is based on the work of Dunne *et al.* (2005), where the equation governing a given class of phytoplankton biomass is

$$\frac{\partial P}{\partial t} = \mu_P P - \lambda \left(\frac{P}{P_*}\right)^a P, \tag{5}$$

where P is the concentration of some class of phytoplankton, μ_P the growth rate, λ the grazing rate, P_* the scale concentration for grazing, and a the grazing parameter ($a = 1$ for classic logistic growth). TOPAZ uses the Dunne *et al.* (2005) values of $P_* = 1.9$ mmol C m^{-3} and $\lambda = 0.19\, e^{KT}/86\,400\, s$. If growth and grazing are approximately in balance, then

$$P \approx \left(\frac{\mu_P}{\lambda}\right)^{1/a} P_*. \tag{6}$$

Hence, different groups of plankton might differ in how they are controlled by nutrients or by how tightly they are controlled by grazing.

TOPAZ distinguishes between three functional groups.

(1) Small plankton: Meant to represent nanoplankton, such as *Synechococcus* and *Prochlorococcus*. This class of phytoplankton has relatively low half-saturation coefficients for iron (5 nM), ammonia (0.2 μM), phosphorus (0.2 μM), and nitrate (2.0 μM). P^C_{max} is set to 2.0×10^{-5} s^{-1}. The grazing exponent a is set to 1, following Dunne *et al.* (2005). This class of phytoplankton is therefore weakly limited by nutrients, but strongly limited by grazing.

(2) Large plankton: Meant to represent green algae, diatoms, and other large phytoplankton. This class of plankton has half-saturation constants for nutrient uptake three times that of small phytoplankton. Additionally, they have the ability to store iron internally. The grazing exponent for large phytoplankton $a = 1/3$, following Section 5.1 of Dunne *et al.*, (2005; this value is also used in Galbraith *et al.*, 2010). Therefore, although the large plankton require much higher levels of nutrient to realize their maximum growth rate, their concentration actually increases as the cube of that growth rate, because they are less tightly limited by grazing. The fraction of large phytoplankton taken to be diatoms is given by

$$F_{diat} = \frac{SiO_4}{K_{Si} + SiO_4}, \tag{7}$$

with $K_{si} = 3$ mmol m^{-3}, so that silicate limitation results in reducing the diatom fraction.

(3) Diazotrophs: Meant to represent organisms that fix nitrogen from N_2, such as *Trichodesmium*. These organisms require four times as much iron as small phytoplankton and have a maximum growth rate of 40% that of small phytoplankton. The grazing exponent is the same as for large phytoplankton. However, although diazotrophs play a critical role in maintaining the nitrogen inventory of the ocean, they represent a relatively small fraction of biomass in our simulations and their dynamics will therefore be ignored for the remainder of this paper.

Then, considering only the scaling between large (Lg) and small (Sm) phytoplankton, we can find two separate regimes. When nutrients or light are extremely limiting (e.g. when $NH_4 \ll K^{Sm}_{NH_4} < K^{Lg}_{NH_4}$), an increase in the limiting nutrient results in the same relative change in the growth rate for small and large phytoplankton. However, because of the different grazing laws, this will result in a proportional increase in the concentration of small phytoplankton $P_{Sm} \propto NH_4$, but a much larger relative increase in the concentration of large phytoplankton $P_{Lg} \propto P^3_{Sm} \propto NH^3_4$. When the concentration of the most limiting nutrient is higher than the half-saturation constant for the small phytoplankton $K^{sm}_{NH_4} < NH_4$, relative changes in the growth rate are bigger for large phytoplankton than for small phytoplankton, so that the ratio of large to small phytoplankton follows an even higher power law. We therefore generally expect to find more variability in large phytoplankton concentration than in small phytoplankton concentration.

Ocean-ice model

The ocean-ice model used in these simulations is the ocean-ice component of the GFDL CM2.1 global coupled climate model (Delworth *et al.*, 2006). The model is configured with 50 vertical layers with thicknesses ranging from 10 m over the top 200 m to a maximum thickness of 250 m at 5500-m depth. The meridional resolution is 1°, whereas the zonal resolution varies between 1° in mid-latitudes and 1/3° at the equator. North of 65°, a tripolar grid is employed to avoid singularity at the north pole. Up-to-date parametrizations of mixed-layer dynamics, isopycnal mixing, advection by subgridscale eddies, bottom topography, bottom flows, and lateral viscosity are included (Griffies *et al.*, 2005; Gnanadesikan *et al.*, 2006). Both the dynamics and thermodynamics of five thickness classes of sea ice are simulated.

Surface forcing is set using the Coordinated Ocean-ice Reference Experiment (CORE) protocol (Griffies *et al.*, 2009), where the inputs for calculating surface fluxes are taken from an atmospheric reanalysis dataset adjusted to agree better with *in situ* measurements. Sensible and latent heat fluxes are then calculated using bulk formulae. These simulations are referred to as the CORE runs. In CORE runs, freshwater forcing is given by a combination of applied precipitation, evaporation computed using bulk fluxes, and a correction diagnosed to restore surface salinities in the top 10 m to climatological monthly values over 60 d. Hence, the fluxes forcing the CORE runs could be thought of as "best guess" observationally based estimates. Such a prescription omits important feedbacks whereby the atmosphere ensures that rainfall and evaporation are consistent with each other, although the restoring correction is a crude representation of these feedbacks. Without it, many models fail to maintain a robust Atlantic Meridional Overturning circulation (see section 16 of Griffies *et al.*, 2009, for further discussion). However, the presence of a restoring correction damps long-period variability in salinity, with implications for biogeochemical cycles. The resulting

difficulty in simulating long-term salinity variability forms an important part of our motivation for examining coupled climate models.

The CORE models are initialized from the World Ocean Atlas database with respect to temperature, salinity, nitrate, phosphate, and silicate. Seven cycles of the 46 years of observed forcing are then applied, comprising a run of 322 years. Although this is insufficient to spin up the deep ocean carbon cycle, surface nutrients, biomass, and productivity come to near-equilibrium rapidly. For example, the average relative change in surface large phytoplankton concentration is less than 3% between the final two cycles and the average total biomass changes by 0–0.8% over depths ranging from 100 m to the surface.

Coupled climate model

In coupled climate models, the incoming solar radiation, atmospheric greenhouse gases, aerosols, and some aspects of the land surface are fixed, but the air–sea fluxes of heat and momentum are then allowed to evolve freely. Hence, the surface fluxes could deviate from the best observationally based fluxes, but they do so in a consistent way (a cool bias will cause a decrease in evaporation, which then results in decreased precipitation). Such models can simulate the mean climate, its forced response to changes in the radiation balance, and its intrinsic variability, but will not simulate the response of climate in any given year. Therefore, the coupled models should be used to match statistical relationships between biological features and physical forcing, not to simulate individual years or decades.

The model used for these runs is the GFDL's ESM2.1. The physical core of this model is the CM2.1 global coupled climate model described in Delworth *et al.* (2006), with the baseline ocean solution described in Gnanadesikan *et al.* (2006). CM2.1 has an atmospheric physical climate that compares well with other global climate models (Reichler and Kim, 2008), an ocean circulation in the Southern Ocean that is quite realistic (Russell *et al.*, 2006), and a relatively realistic *El Niño*–Southern Oscillation (van Oldenborgh *et al.*, 2005; Wittenberg *et al.*, 2006). Ocean temperature and salinity in ESM2.1 are initialized from the CM2.1 1860 control run after 2000 years of run. Ocean nutrients in ESM2.1 are initialized from the World Ocean Atlas, then run with interactive chlorophyll and an interactive land biosphere, but with radiative gases at 1860 levels for another 1600 years. Output is then taken from the last century of this simulation. Variability seen in the coupled model, therefore, should reflect the background level of unforced, internal variability in the climate system.

Results

Model evaluation

Differences between the models are summarized in Figure 1, and a statistical comparison of the temperature, salinity, phosphate, nitrate, and the natural log of surface chlorophyll to observations is presented in Table 1. Zonally averaged errors in sea surface temperature (SST; black solid line, Figure 1a) reveal a strong warm bias in the Southern Ocean resulting from an excess of summer shortwave radiation and a cold bias elsewhere in ESM2.1. The low-latitude cold bias probably contributes to lower evaporation rates and a fresh bias (red solid line, Figure 1a). The CORE model tends to be biased cold (dashed black line, Figure 1a) and slightly salty (dashed red line, Figure 1a), illustrating the limits of the restoring correction in

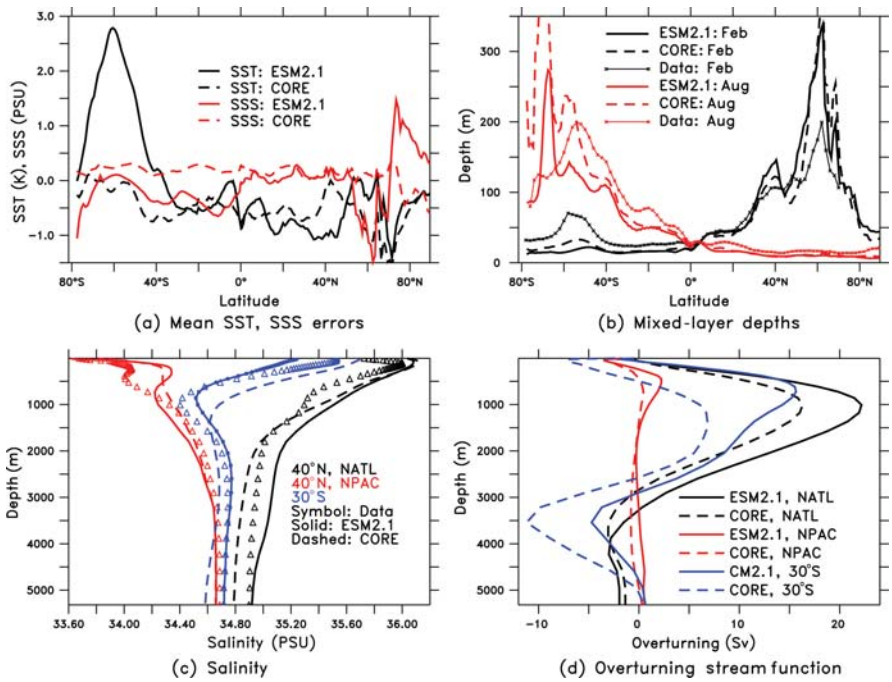

Figure 1. Evaluation of the physical circulation in the ESM2.1 (thick solid lines) and CORE (thick dashed lines). (a) Zonally and annually averaged surface temperature biases. (b) February (black) and August (red) mixed-layer depths zonally averaged over all basins. Averaged mixed-layer depth from de Boyer Montegut *et al.* (2007) is illustrated with the thin line and symbols. (c) Zonally averaged profiles of salinity at 40°N in the North Atlantic (black), 40°N in the North Pacific (red), and 30°S across the entire Southern Ocean (blue). (d) Overturning stream function at 40°N in the North Atlantic (black), 40°N in the North Pacific (red), and 30°S in the Southern Ocean (blue).

Table 1. Statistical measures of model performance compared with observations for surface and entire water column.

Field	CORE	ESM2.1
SST	**0.998**, 0.989, *0.84*, −0.50	**0.99**, 0.92, *1.43*, −0.08
SSS	**0.98**, 1.01, *0.38*, 0.18	**0.88**, 1.04, *0.85*, −0.15
Surface PO_4 (80°S–70°N)	**0.96**, 0.97, *0.18*, 0.033	**0.91**, 0.96, *0.24*, −0.037
Surface NO_3 (80°S–70°N)	**0.97**, 0.99, *2.32*, −0.26	**0.94**, 0.86, *3.18*, −0.73
ln(Chl) (70°S–70°N)	**0.73**, 1.11, *0.29*, −0.08	**0.72**, 0.83, *0.25*, −0.09
Temperature (three-dimensional)	**0.99**, 1.02, *0.82*, 0.31	**0.98,** 0.96, *1.21*, 0.84
Salinity (three-dimensional)	**0.94**, 1.10, *0.18*, −0.001	**0.92**, 1.13, *0.20*, −0.001
PO_4 (three-dimensional)	**0.93**, 1.05, *0.23*, 0.00	**0.84**, 1.13, *0.39*, 0.00
NO_3 (three-dimensional)	**0.83**, 1.05, *5.7*, −2.0	**0.76**, 0.89, *7.7*, −4.7

Correlations are displayed emboldened, relative standard deviation (model/observed) in regular type, RMS error in italics, and mean bias underlined.

actually fixing surface salinities to observations. The RMS temperature error of 1.43°C is only slightly larger than the 1.28°C seen in the 1990 control run of the CM2.1 coupled climate model by Gnanadesikan *et al.* (2006), and is essentially identical with CM2.1 without interactive biology when it is run for 1600 years. The changes in ocean shortwave absorption and land hydrology induced by including prognostic biology do not significantly alter the earlier published solution. The three-dimensional temperature and salinity fields match the data slightly better than the Max Planck Institute (MPI), National Center for Atmospheric Research (NCAR), and Institut Pierre et Simon Laplace (IPSL) models reported in Schneider *et al.* (2008).

The annual cycle of zonally averaged mixed-layer depth (Figure 1b) demonstrates that the models capture the range of mixed-layer depth in mid-latitudes, but tend to have deeper mixed layers in winter high latitudes (particularly in the North Atlantic and the Southern Ocean) than observed. Summer mixed layers are close to observational values in the northern hemisphere, but tend to be too shallow in the Southern Ocean in both models.

Examining profiles of salinity at a number of locations (Figure 1c), we find that both models capture the contrast between the salty North Atlantic (black lines) and the fresh North Pacific (red lines), with the Southern Ocean lying in between the two. ESM2.1 also predicts distinct salinity minima at about the right depth in the North Pacific and Southern Ocean, though both locations are too salty. The CORE model in contrast (dashed lines) fails to reproduce these salinity minima seen in both the North Pacific and Southern Ocean, suggesting an overly weak formation of mode and intermediate waters, but a flushing of the deep ocean with cold, fresh bottom water, consistent with overly high mixed-layer depths in the Southern Ocean.

Differences in the circulation of Antarctic Bottom Water are reflected in the overturning stream function at 30°S (blue lines, Figure 1d). AABW export is extremely weak in ESM2.1 (as it is in all the CM2.1 series), but reaches 11.2 Sv in the CORE runs, with ~4.3 Sv in the Atlantic basin. This circulation fails to upwell in the North Pacific in either the CORE or ESM2.1 simulations (red lines, Figure 1d), though the ESM2.1 model does indicate an overturning cell above 1000 m consistent with the formation of the North Pacific Intermediate Water salinity minimum. Both models demonstrate a significant North Atlantic overturning, with ESM2.1 predicting a somewhat deeper maximum of 23.5 Sv, whereas the CORE simulation gives 16.9 Sv.

The best-characterized biogeochemical fields with which the models can be compared are the spatial distribution of macronutrients. As indicated by the thick black dashed line in Figure 2a, the CORE ocean-ice model captures the large-scale distribution of surface phosphate and nitrate, with higher values along the equator, higher values in the northern Subpolar Gyres, and the highest values in the Southern Ocean. The model also captures the tendency towards nitrate limitation that allows for unutilized phosphate in the Subtropical Gyres, where nitrate essentially declines to zero (red lines). Correlations with observed surface nutrients exceed 0.95. The main error visible in Figure 2a is the underestimate of surface phosphate in the northern oceans, which is notably worse in ESM2.1 than in the CORE model. Profiles of nutrients in the North Pacific (red lines, Figure 2b) demonstrate that the phosphate deficit penetrates to much greater depths, possibly reflecting the lack of deep upwelling seen in Figure 1d. The CORE model has a much reduced bias in phosphate concentration in the North Pacific, possibly because of the lack of deep upwelling is balanced by a lack of lateral export (reflected in the lack of 1000 m salinity minimum in Figure 1c) and possibly because it has only been run for one-fifth the time as ESM2.1. The three-dimensional correlation of phosphate with observations in ESM2.1 (0.84) is comparable with the 0.82–0.86 reported by Schneider *et al.* (2008) for the NCAR, MPIM, and IPSL models. The three-dimensional correlation with nitrate is lower than for phosphate and nitrate is biased low globally. This is because the oxygen minimum zones become too intense in this model, resulting in overly intense denitrification. Because surface nutrients are relatively realistic, however, we suspect that the overly high rates of denitrification are being compensated by excessive nitrogen fixation.

Additional constraints on the model can be gleaned by comparing with products inferred from satellite remote sensing. The zonal integral of chlorophyll (Figure 2c), which is very similar between the ocean-only and coupled models, tends to underestimate the total chlorophyll inventory in part because of a failure to capture very high values in upwelling zones. The chlorophyll signal indicates that low simulated surface nutrients in high northern latitudes are not because of an excess of productivity, suggesting that insufficient nutrient supply might be responsible. Both the CORE and ESM2.1 simulations capture approximately half of the observed spatial variance in the log of annually averaged chlorophyll with an underestimate of ~8% globally (Table 1). Zonal-mean primary productivity is essentially identical with that estimated from SeaWiFS chlorophyll using the Carr (2002) algorithm (Figure 2d) in both the ocean-only and coupled models. However, given that the differences between the models and observational estimates are considerably smaller than that between individual observational estimates (Gnanadesikan *et al.*, 2004) and less than the uncertainty in chlorophyll retrievals, the agreement might be fortuitous.

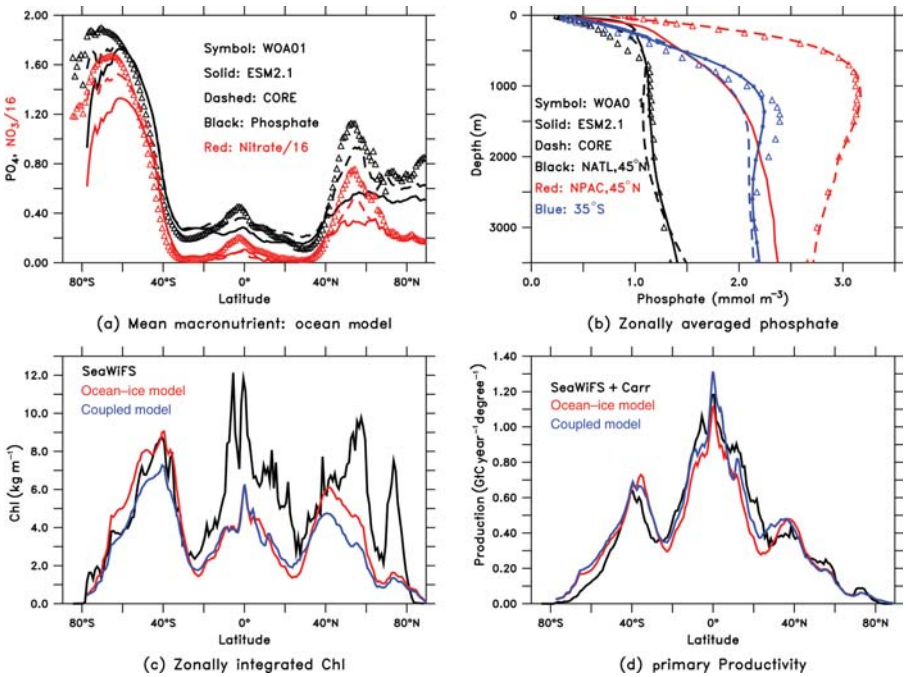

Figure 2. Evaluation of model fidelity. (a) Annual mean surface phosphate (black) and nitrate/16 (red) from data (WOA01, Conkright *et al.*, 2002, symbols), ESM2.1 (solid lines) and CORE (dashed lines). (b) Zonally averaged phosphate over the top 1500 m. Symbols are data, black lines an average within the North Atlantic, red lines an average within the North Pacific, and blue lines an average across the Southern Ocean. (c) Zonally integrated chlorophyll from the SeaWiFS satellite (black) compared with surface chlorophyll from the models. (d) Primary productivity compared with that estimated from the SeaWiFS satellite using the algorithm of Carr (2002).

Size structure and the disproportionate variability of large phytoplankton

We begin by examining the relative interannual variability of a number of fields, using the coefficient of variation (s.d./mean) of the annually smoothed field as a metric. For the first 7 years of the SeaWiFS mission, the coefficients of variation in chlorophyll (Figure 3a) and productivity (Figure 3b) are <0.1 over most of the global ocean. Assuming purely sinusoidal variation, a coefficient of variation of 0.1 would imply variation from 0.86 to 1.14 times the mean value. The largest relative variability is observed not in the centre of the high-chlorophyll equatorial upwelling or Subpolar Gyres, but instead along the edges. A similar observation was made by Martinez *et al.* (2009) when examining interdecadal variability of chlorophyll while comparing SeaWiFS and CZCS satellite products. Comparing the short SeaWiFS time-series with the last 46-year cycle of the CORE-forced runs, we find a similar concentration of interannual variability along the edges of the equatorial cold tongue and at the edges of the Subtropical Gyres. The coefficient of variation for modelled productivity is generally smaller than for modelled chlorophyll, though the spatial patterns of the log of the variation are correlated with a coefficient of 0.76. As indicated by the regression coefficient in the lower right of Figure 3d, a 10% change in model chlorophyll would only be expected to produce a 5.2% change in productivity. A similar power-law dependence is found in algorithms for estimating primary productivity from satellite-estimated chlorophyll (compare Figure 3a and b), because higher chlorophyll results in higher light-harvesting capacity, but also less penetration of solar radiation.

As might be expected from Equation (6), the models predict very different variability for the biomass of large and small phytoplankton. Over most of the ocean, the coefficient of variation in small phytoplankton biomass (Figure 3e) is less than 10%, much smaller than for total chlorophyll. The pattern of chlorophyll variability is correlated with the changes in small biomass, with a correlation coefficient of 0.58 in the CORE run. However, a 10% change in chlorophyll only results in a 1.8% change in small plankton biomass. In contrast, the coefficient of variation for large plankton biomass (Figure 3f) is comparable with (and along the equatorial cold tongue much larger than) the coefficient of variation in chlorophyll. Therefore, the bulk of the variability in productivity is in the large phytoplankton, not the small, although small plankton make up the majority of the global phytoplankton biomass. The coupled model (not presented) exhibits similar patterns of variability as the CORE-forced simulation, with much more variability in large phytoplankton, similar correlation and regression coefficients between chlorophyll and other fields, and the largest-amplitude variability at the edge of the Subtropical Gyres and coastal upwelling regions.

Comparing the zonal average of the coefficient of variation in large phytoplankton biomass on interannual time-scales (Figure 4a) further emphasizes the difference between small and large phytoplankton. The standard deviation of the total biomass (thin lines) is on average less than 10% of the mean over almost the entire ocean in both the ocean-only and coupled models. In contrast, for large biomass (thick lines) over the tropics, a relative standard deviation of 35% is seen in both models. Interannual variability in the diatom biomass (symbols, Figure 4) largely tracks that of large phytoplankton biomass in the CORE runs (this variable was not saved for the ESM2.1 runs).

Variability in the annual productivity is not, however, the only possible way that biogeochemical variability can project into

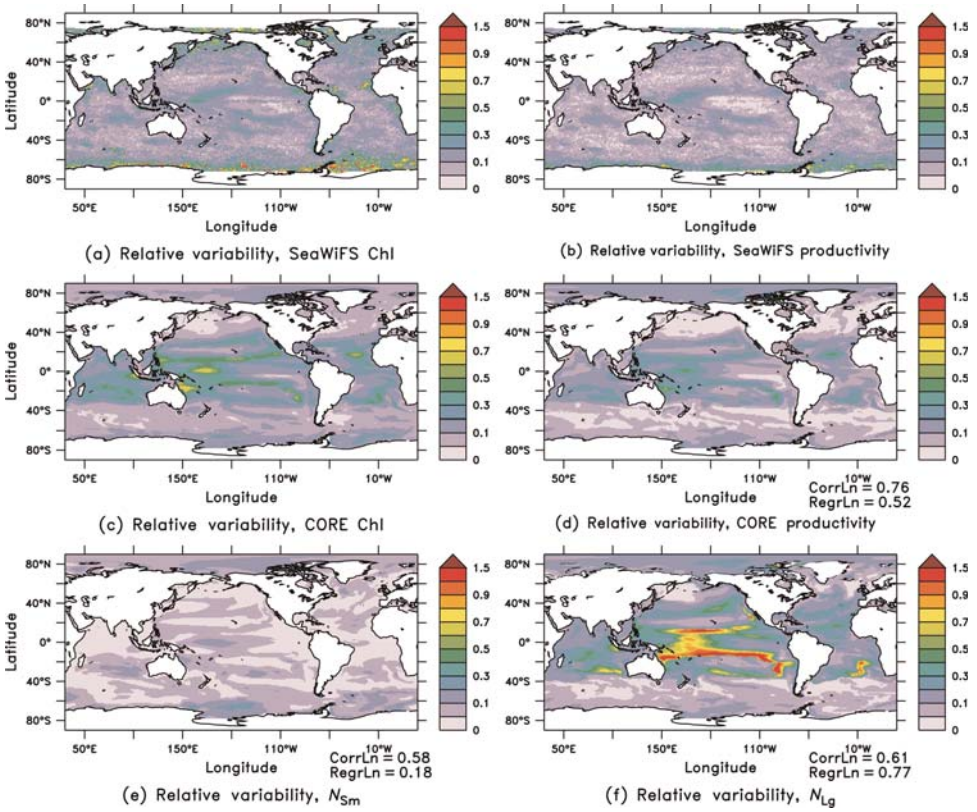

Figure 3. Coefficients of variability (standard deviation of 12-month running smoothed/mean) for quantities estimated from satellite and computed in a CORE-forced (Griffies *et al.*, 2009) ocean-ice model. Contours are at values of 0, 0.05, 0.1 to 1 by 0.1, and 1.5. Correlations and regressions between the natural log of chlorophyll and the natural log of the relevant quantity are illustrated to give a sense of power-law relationships for the model output. (a) Surface chlorophyll, SeaWiFS. (b) Primary productivity from SeaWiFS using the Carr (2002) algorithm. (c) Modelled surface chlorophyll. (d) Modelled productivity (total grazing 0–100 m). (e) Modelled small phytoplankton biomass (0–100 m). (f) Modelled large phytoplankton biomass (0–100 m).

interannual changes in ecosystems. The "match–mismatch" hypothesis of Cushing (1990) builds on the classic work of Hjort (1914), suggesting that changes in the timing of spring bloom are more important than that in the magnitude of productivity. Analysing interannual variability in productivity month by month, with a particular focus on the spring bloom, we find that the models predict more variability in spring. During April, the coefficients of variation in total plankton biomass, diatom biomass, and large plankton biomass all increase in high northern latitudes. The largest change is seen for large plankton biomass between 60 and 80°N (dashed lines), where the coefficient of variation increases from 0.10–0.12 in the annual mean to ~0.5 during April in the CORE model and 0.75–0.80 during April in ESM2.1. In contrast, the coefficient of variation increases from ~0.3 in the annual mean to ~0.4 for April alone for large phytoplankton in the tropics, a much smaller increase. Relative variability remains reasonably low in April throughout the southern hemisphere. Roughly the opposite geographic pattern is seen in the austral spring (October, Figure 4d), with the average coefficient of variation in large biomass reaching 0.7 at some latitudes in the southern hemisphere. Again, we note that the CORE model tends to have less variability than ESM2.1 at high latitudes and a little more variability in the tropics. July (Figure 4c) looks more like the interannual variability, with a tropical peak and lower values in the high latitudes. The actual values for July are higher, because the mean coefficient from 30°S to 30°N is 0.35 in ESM2.1 during July vs. 0.24 in the annually smoothed version, but this is a much smaller increase than that observed in spring at high latitudes. As discussed below, changes in the timing of productivity during the year are most important at high latitudes, whereas in low latitudes interannual changes in the annual mean productivity are much more important.

As illustrated in Figure 5, the basic spatial pattern of interannual variability in spring large phytoplankton biomass in ESM2.1 resembles that observed for chlorophyll, but with a much greater range. As with the SeaWiFS annual data, regions of high variability are observed at the boundary between the Subtropical Gyre and the high-nutrient equatorial zone, but also in mode-water formation regions where deep mixed layers are found along the boundary of the Subtropical and Subpolar Gyres. High variability is also found in convective regions within the Subpolar Weddell Sea, Bering Sea, and North Atlantic. The difference between the left- and the right-hand columns of Figure 5 reinforces the result from Figures 3 and 4 that chlorophyll or total biomass alone can give an inaccurate picture of the interannual variability within an ecosystem.

Therefore, the three key results of this section are that large plankton and diatoms vary more than small plankton, that large

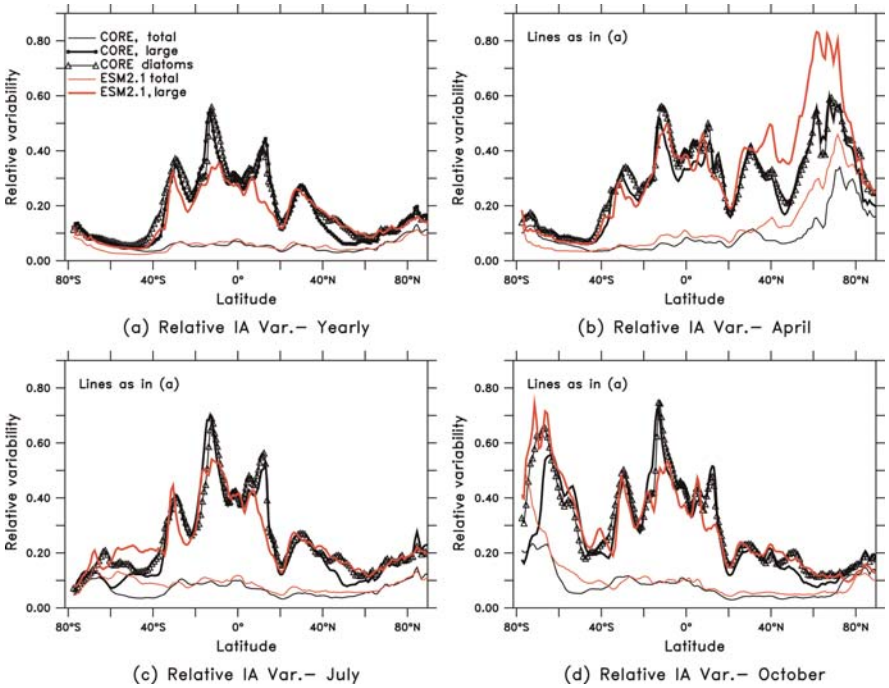

Figure 4. Zonally averaged coefficient of variation in phytoplankton biomass (standard deviation/mean) as a function of space and time. Dashed lines are for years 401–500 of ESM2.1, solid for the CORE-forced run. Thin lines are for total phytoplankton biomass, thick lines are for large phytoplankton biomass alone, and symbols are for diatom biomass. (a) Variability of 12-month smoothed biomass. (b) Same as (a) but only for April. (c) Same as (a) but only for July. (d) Same as (a) but only for October.

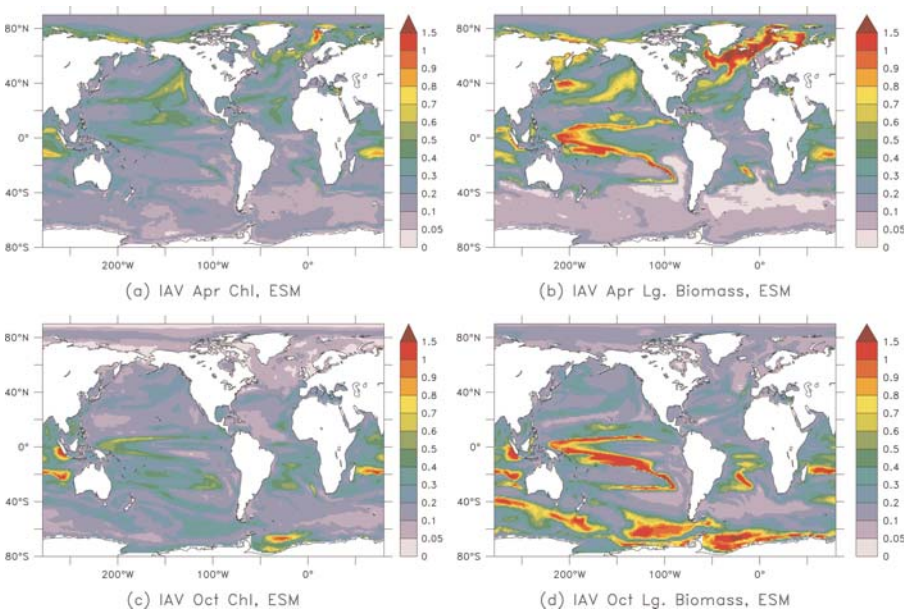

Figure 5. Interannual variability in spring/autumn for ESM2.1. All plots display standard deviation over mean. (a) Surface chlorophyll, April; (b) large phytoplankton biomass, April; (c) surface chlorophyll, October; and (d) large phytoplankton biomass, October.

relative variability is found on the edges of highly productive regions, and that relative variability during the spring bloom is larger than variability over the entire year. The following section expands upon the second of these results, looking at the boundary between the equatorial upwelling and the Subtropical Gyre, indicating that the changes in concentration are associated with that in the areal extent of the oligotrophic gyre and considering the physical forcing driving such changes. The section "Variability in

large phytoplankton biomass in the North Pacific during boreal spring" examines mechanisms behind spring variation in large phytoplankton concentrations in four regions: the Subtropical Gyre off Hawaii, the Kuroshio extension, the Sea of Okhotsk, and the western Bering Sea. Because interannual variability in diatoms largely tracks these variations in the CORE-forced runs in these regions, we expect the results to be qualitatively applicable to diatoms as well.

Interannual changes in biome area: the case of the equatorial upwelling zone

We begin with the equatorial Pacific where interannual variability is high and breaking down this variation month by month yields less of an increase (Figure 4) than at high latitudes. The variability in this region is relatively consistent between the CORE and ESM2.1 runs. Both models simulate the largest variability around the edge of the high-nutrient cold tongue, a picture similar to that displayed in Figure 3a and in the work of Martinez *et al.* (2009). If we define the boundary between the equatorial upwelling biome and oligotrophic gyre/subtropical biome either using the Chl = 0.07 mg m^{-3} isoline (following Polovina *et al.*, 2008) or the NO_3 = 0.02 mmol m^{-3} line (Figure 6a) between 20°S and 20°N, we note that the CORE model indicates the gyres expanding and contracting with decadal and interannual frequencies. Although nitrate is only one of the sources of nitrogen for the off-equatorial regions in this model, it is used as an indicator of upwelled nutrient. The changes in the oligotrophic gyre area can be regressed onto changes in chlorophyll (shading, Figure 6b), revealing that a larger oligotrophic gyre area is associated with lower chlorophyll concentrations at the edge of the high-nutrient waters. Regressing the gyre area against windstresses (arrows, Figure 6b) demonstrates that larger oligotrophic gyre areas are associated with anomalous westerlies along the gyre margins. The correlation between equatorial winds and the tropical oligotrophic gyre area over this period is 0.77, whereas off-equator, the correlations approach 0.85.

We examined the mechanistic connection between winds, currents, and the area of the subtropical biome by looking at the mass balance of nitrogen in the CORE runs in three areas outlined by the boxes in Figure 6b. Changes in nitrate import that explain a large fraction of changes in the vertical particle export flux can be identified as important causative agents for export flux variability. Which fluxes are the most important end up being slightly different for the regions on and off the equator. Along the equator (175°E–160°W 3°S–3°N), the anomalous advection of nitrate from below and from the east together (dashed/red line, Figure 7a) correlate well with the particle export anomaly at 100 m (solid/black line, Figure 7a). However, this correlation is not simply because of the direct response of wind-driven currents acting on the background nutrient field. The flux resulting from changes in currents alone (dotted/blue line, Figure 7a) has a strikingly lower correlation with the particle export (0.36 vs. 0.9) and a lower amplitude of variability. In the northern centre of action (165–140°W 5–15°N), the dominant control of the particle export is from advection of nutrient into the region from the south (compare solid/black and dashed/red lines, Figure 7b). Here too, however, changes in the velocity alone account for only a small part of the variability, implying that changes in the

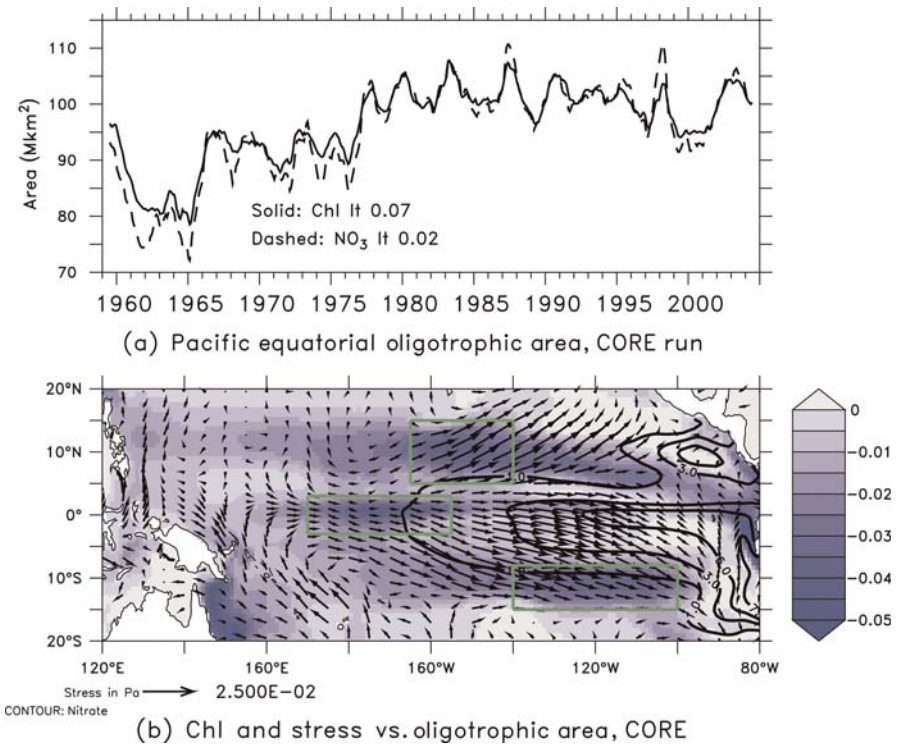

Figure 6. Changes in the oligotrophic gyre area in the central Pacific (20°N–20°S, following definition of Polovina *et al.*, 2008). (a) Changes in the oligotrophic gyre area in the CORE-forced model defined using chlorophyll (solid) and the corresponding area of low nutrients (dashed). (b) Changes in surface chlorophyll (shading) and on windstress (arrows) corresponding to a 1 s.d. change in the gyre area. Contours indicate mean surface nitrate.

nutrient concentrations of the inflow are dominant. The dominance both of north–south advection and of changes in nutrient concentrations in explaining such changes in advective flux is also found in the region from 140 to 100°W and 8 to 15°S (Figure 7c). This region covers the southern centre of action in Figure 6b (although the dotted blue and solid black lines do not appear well correlated, they in fact match up extremely well until the 1980s). In all three regions, the changes in export represent changes in the regional extent of the highly productive, nutrient-rich waters, not just local changes in productivity. This implies that predicting the change in the biome area involves more than just predicting changes in the amplitude of ENSO; the changes in the background field of nutrients must also be understood.

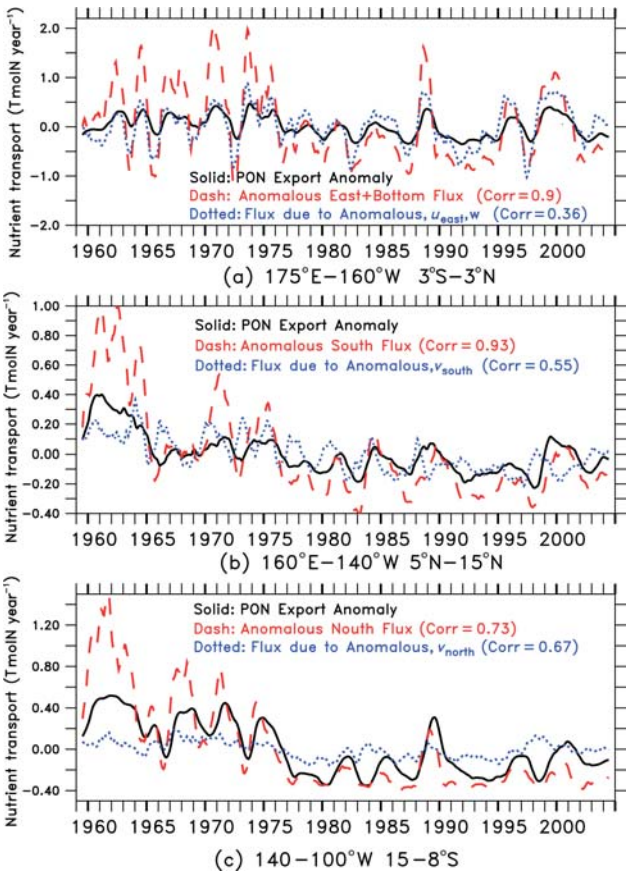

Figure 7. Time-series of anomalous export of particulate organic nitrogen (black lines), advective fluxes of nitrate (dashed), and advective fluxes because of changes in velocity alone (dotted) for the three centres of action in Figure 6. (a) 175°E–160°W 3°S–3°N, (b) 160–140°W 5–15°N, and (c) 140–100°W 15–8°S.

Variability in large phytoplankton biomass in the North Pacific during boreal spring

Identification of different regimes

Turning to variability associated with the spring bloom, we note that the relationship between local SST and biological cycling during April reveals a complicated pattern in the North Pacific (Figure 8a and b). The correlation patterns of chlorophyll and large plankton biomass with SST (shading) reveals a rough consistency, with a tongue of high variability negatively correlated with SST extending from the centre of the Subtropical Gyre to the northeast off the Pacific coast of Canada, weak positive correlation in the northwest Pacific, stronger positive correlation in the Sea of Okhotsk, and a region of strong negative correlation in the western Bering Sea off Kamchatka. However, the coefficients of variation in chlorophyll and large phytoplankton biomass (contours) are only of similar magnitude in the first of these regions. In the region from 150 to 160°E and 36 to 40°N (in the Kuroshio extension), the coefficient of variation in chlorophyll is 0.35, as opposed to 0.98 for large phytoplankton biomass; similar differences are found in the Sea of Okhotsk and western Bering Sea. In all four regions (but particularly those outside the Subtropical Gyre), the coefficient of variation in large biomass during April is larger than during either March, May, or the entire period from March to May. In the Kuroshio extension, for example, the coefficient of variation for large phytoplankton biomass during the entire March–May period is only 0.24, approximately one-fourth that of the April period alone. Such differences are consistent with the interannual variability in April biomass being primarily driven by variability in bloom timing, rather than reflecting interannual changes in the magnitude of seasonal productivity. As discussed in the following sections, the physical mechanisms underlying this variability differ in each of the regimes denoted by the green boxes in Figure 8.

The drivers of variation in large phytoplankton biomass during April are analysed by correlating this variability with SST, SSS, the

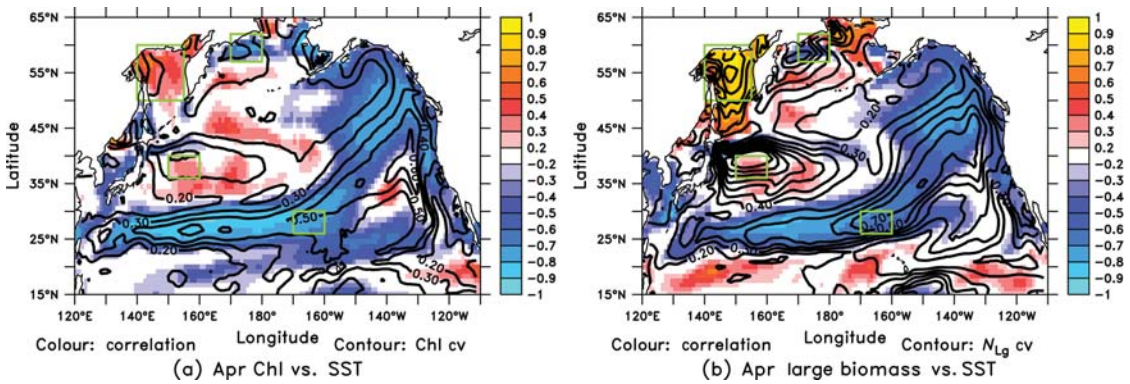

Figure 8. Relationship of variability in local SST with variability in (a) chlorophyll and (b) large phytoplankton biomass during April in the North Pacific. Colours indicate correlation coefficients, contours the coefficient of variability as in Figure 5.

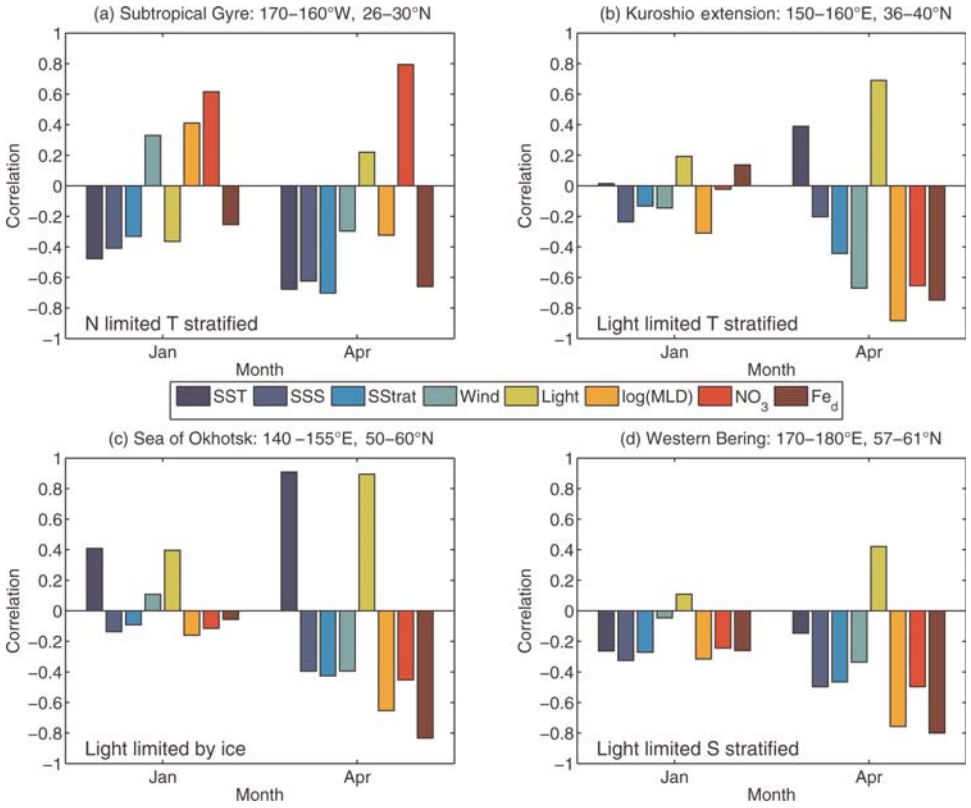

Figure 9. Large phytoplankton biomass during April correlated with other fields during 2 months (January and April) in the four different dynamic regimes in the North Pacific denoted by the green boxes in Figure 8. From left to right, each set of bars shows: SST, sea surface temperature; SSS, sea surface salinity; Sstrat, salinity difference between 0 and 150 m; Wind, magnitude of surface winds; Light, averaged photosynthetically active radiation in mixed layer; log(MLD), logarithm of mixed layer depth; NO_3, nitrate concentration; Fe_d, dissolved iron concentration. (a) Subtropical Gyre, 170 – 160°W 26 – 30°N. Dominant correlation is with nitrate both at zero lag and with a 3-month lead. (b) The Kuroshio extension region, 150 – 160°E 36 – 40°N. Note strong correlation with light, anticorrelation with wind, and mixed-layer depth at zero lag. (c) Sea of Okhotsk. Note high correlation at zero lag with mixed-layer light and temperature, but low correlation with sea ice. (d) Western Bering Sea. Note strong anticorrelation with mixed-layer depth and positive correlation with light at zero lag.

salinity difference between the surface and 150 m, windspeed, averaged photosynthetically active radiation in the mixed layer, the natural log of the mixed-layer depth, nitrate, and dissolved iron concentrations (Figure 9) for each of the boxes in Figure 8. Correlations with April conditions (right-hand set of bars in each panel in Figure 9) are illustrated to isolate the mechanisms driving the interannual changes in biomass, whereas correlations with January conditions (left-hand set of bars in each panel) are displayed to isolate whether the environmental controls are potentially predictable from oceanic conditions earlier in the year.

The Subtropical Gyre

In the Subtropical Gyres, downwelling and high vertical gradients in temperature combine to create regions with low surface nutrients. Although sometimes referred to as biological deserts, these regions do support some pelagic fisheries. In such nutrient-limited, low-latitude regimes, one would expect surface cooling to result in more mixing, greater nutrient supply, and hence higher productivity. The mixed-layer depth would therefore be expected to be correlated positively with biomass and chlorophyll in tropical and subtropical regions. Follows and Dutkewicz (2002) compared a model forced in a similar manner to ours with SeaWiFS chlorophyll in the subtropics. The modelled mixed-layer depth was correlated positively with observed chlorophyll, supporting the idea that the increased chlorophyll was associated with increased vertical supply of nutrients.

Examining the subtropical North Pacific near Hawaii, from 170 to 160°W and 26 to 30°N, we find a basic consistency with the classic picture (Figure 9a). During April, large phytoplankton biomass is best correlated with high levels of nitrate and inversely correlated with SST. However, the deep mixed layers during April are apparently not necessary for high biomass during the same month. Instead, high phytoplankton biomass during April is (weakly) associated with shallower mixed layers, higher light, and weaker winds. A correlation between April biomass and deeper mixed layers (associated with higher winds and cooler SSTs) only appears when the previous January is considered. That the correlation between April large biomass and January mixed-layer depth is smaller in magnitude than the anticorrelation with temperature also suggests that some of the variability in nutrient might result from southward advection of colder, fresher northern waters and not just to deeper local mixing. The negative correlation with iron indicates that iron cannot be the dominant limiting nutrient, but is instead drawn down more by high levels of biological activity. Because we model nutrient limitation using Liebig's law of the minimum [Equations (1) and (4)], iron limitation in this version of our model only has an impact when it is less limiting that nitrogen, which only occurs in the

Southern Ocean, in the Peru upwelling, and the Pacific cold tongue.

The Kuroshio extension: a mode-water formation region

Farther north, we find a region that has a strong seasonal cycle in mixed-layer depth at the edge of the Subtropical Gyre. Deeper winter mixing means that spring light limitation can be extreme in this region, which is associated with formation of key mode waters. Nutrients in the Kuroshio extension are more abundant than in the Subtropical Gyre, though at lower levels than in the Subpolar Gyre, with the result that chlorophyll levels are somewhat lower than in the Subpolar Gyre. Sarmiento *et al.* (2004) defined this region as a combination of the subtropical seasonal stratified biome and Subpolar Gyre biome, whereas Polovina *et al.* (2011) include it in the temperate biome. As demonstrated in Figures 8b and 9b, the large interannual variability in April large phytoplankton biomass in this region is only weakly correlated with temperature, but is very strongly anticorrelated with mixed-layer depth and positively correlated with mixed-layer light availability. Light limitation, rather than nutrient limitation, plays a dominant role here, so that the spring bloom coincides with the shallowing of the mixed layer. Note that there is no nutrient limitation during April, despite the annual mean nutrient concentrations being somewhat low in this area (Figure 2a), so that such (unrealistic) limitation kicks in later during summer. Shallow mixed layers can result from low winds (hence the anticorrelation with wind). They can also be associated with either local warming or from the advection of fresher, colder waters from the north, hence the weak correlation with SST. In contrast to the centre of the Subtropical Gyre, this region displays relatively little correlation with conditions in January, suggesting that it will be challenging to predict.

The Sea of Okhotsk: a marginal ice zone biome

A third region outlined in Figure 8 is the Sea of Okhotsk, which is ice-covered during winter and, as such, was classified by Sarmiento *et al.* (2004) as part of the marginal ice zone biome. Interannual variability of large phytoplankton biomass in this region is strongly correlated with temperature and light availability, but only weakly anticorrelated with the mixed-layer depth (Figure 9c). The correlation between April large phytoplankton biomass and sea-ice concentration (not presented) is −0.72, comparable with the 0.86 correlation with mixed-layer light. This is consistent with variability in the timing of ice breakup being important for allowing relief of light limitation and drawdown of surface nutrient and with higher SSTs being associated with this breakup.

The correlation between mixed-layer light and chlorophyll in this region (0.50, not presented) is much lower than the correlation between mixed-layer light and both large and small phytoplankton biomass (0.86). The correlation is lower because the phytoplankton in the TOPAZ model adapt to light availability, reducing their chlorophyll to carbon ratio as more light becomes available [Equation (4)]. As a result, the chlorophyll:carbon ratio in the Sea of Okhotsk during April is strongly anticorrelated with mixed-layer light (−0.63), reducing the amplitude of chlorophyll variability and demonstrating again why it is necessary to be cautious in extrapolating from satellite chlorophyll to ecosystem state.

The Western Bering Sea: a salinity-stratified subpolar biome

A final region of interest is found in the western Bering Sea, where there is large interannual variability in large phytoplankton biomass, but an anticorrelation with temperature. As illustrated in Figure 9d, this region is also light-limited and large phytoplankton biomass is strongly anticorrelated with mixed-layer depth. The anticorrelation with temperature (implying that cold temperatures are correlated with shallow mixed layers) is in contrast to the Kuroshio extension and the Sea of Okhotsk and implies that salinity rather than temperature is the dominant mechanism establishing mixed-layer stratification in this region. This dynamic regime is also found in many other parts of the model ocean, including the southern Labrador Sea, central Norwegian Sea, and Weddell Sea.

The mechanisms by which such salinity anomalies develop are potentially complicated. Gargett (1997) looked at salmon stocks in the North Pacific and argued that the key variable for explaining coastal stability was Alaskan streamflow, which freshened coastal regions and was tied to the changes in low pressure associated with the PDO. However, other analyses we have done using the CM2.1 model suggest that the dominant driver of salinity variability is not the supply of freshwater, but rather the upwelling of saline deep water from below, because of local changes in the windstress curl in our modelled Bering Sea. Galbraith *et al.* (in press) look at similar salinity anomalies in a coarse-resolution coupled model in the Southern Ocean and find that the source of the anomalies is a combination of precipitation anomalies and entrainment of more-saline deep waters.

Discussion and conclusions

The coupled physical–biogeochemical models used to assess climate-change impacts on ocean ecosystems offer insights into how changing prey availability for fisheries could be linked to climate. We review these insights below and consider the potential implications for predicting and diagnosing marine ecosystem variability.

The importance of size structure

The first major message of this paper is that one should not expect a straightforward scaling between primary productivity or chlorophyll and the biomass of the large phytoplankton that are considered most important for fisheries. Over much of the ocean, large plankton apparently respond disproportionately to changes in environmental conditions, driven by differential uptake of nutrients and a size-dependent grazing parametrization (Figures 2d, 3–5, and 8). Because photoadaptation causes the Chl:C ratio to decline as more light becomes available, light-limited regions display much less variability in chlorophyll than in large plankton biomass. This suggests that to track prey availability, fisheries oceanographers should look to satellite estimates of phytoplankton carbon biomass (such as that proposed by Behrenfeld *et al.*, 2005), as well as those that separate out phytoplankton into different size classes (Kostadinov *et al.*, 2009; Mouw and Yoder, 2010). Algorithms for isolating the diatom component (e.g. Alvain *et al.*, 2008) might be important as well. Although diatoms are well correlated with large phytoplankton biomass in one of our runs, there are some differences in detail regarding the location of maximum variability. Moreover, our parametrization of diatom fraction is crude. Although these

products remain preliminary, the fisheries oceanography community should consider using them, especially where results from chlorophyll or primary productivity seem to contradict inferences made from looking at fisheries data. Additionally, when examining simulations from earth system models, fisheries oceanographers should request size structured biomass, which is often simulated by such models, and not be content with modelled chlorophyll or primary productivity.

The potential importance of timing

The second key message of this paper is that models reveal greater variation in the interannual variability of phytoplankton biomass associated with the spring bloom than in the interannual variability in annually averaged phytoplankton biomass. For high-latitude regions when large phytoplankton are considered in isolation the difference can approach an order of magnitude, supporting the Hjort–Cushing "match–mismatch" hypothesis. Larger variability in bloom timing relative to interannually integrated production has been observed in individual ecosystems (Henson and Thomas, 2007; Hunt *et al.*, 2008), but this study breaks new ground in examining the global distribution of the coefficient of variation in large phytoplankton biomass during spring. Variability in bloom timing has potentially important implications for fisheries oceanographers using models such as Ecopath that often either use annual integrated primary productivity (Guénette *et al.*, 2006) or diagnose this quantity from lower trophic level biomass (Piroddi *et al.*, 2010). Our results suggest that such models should probably consider bloom timing if they are to estimate the range of climate-forced ecosystem variability properly.

Bloom timing might be particularly important for understanding different climate responses between "capital breeders" that build up a large stock of resources before breeding and "income breeders" that match food and breeding (Jonsson, 1997). For example, Boulcott and Wright (2008) argue that variability in the timing of blooms in the North Sea has a particularly strong impact on the regional distribution of sandeels. Insofar as income breeders average over the entire seasonal cycle, by contrast, they might be less vulnerable to such variability, as noted by Martin and Wiebe (2004) for Arctic and alpine birds and for Japanese anchovy as opposed to Japanese sardine (A. Takasuka, National Research Institute for Fisheries Science, Yokohama, Japan, pers. comm.). Understanding such trade-offs could be a fruitful area of collaboration between biogeochemical modellers and fisheries oceanographers.

Changes in tropical biome extent: implications for predictability

Both observations and models (Figures 3, 5) exhibit larger relative variability on the edges rather than in the centres of highly productive regions. This could be important, because many organisms have planktonic larval stages and many of the highly productive regions (in particular coastal and equatorial upwelling zones) are divergent. Larvae spawned in such regions might therefore be carried out of them on time-scales of a few weeks and whether they can return might depend more on the food they find on the edges of the unproductive gyres than in the centre of the upwelling regions. We suggest additional investigations to verify whether larval survival within these edge regions is important for certain species. Additionally, the edges of high-productivity regions might be more favourable for visual predators, such as tuna, which could trade-off the requirement for relatively clear water to detect and catch prey with higher prey densities in more turbid waters (Kirby *et al.*, 2000).

Variations at the edges of the gyres have been linked to climate change by Polovina *et al.* (2008), who observed an increase in the area of the oligotrophic gyres during the SeaWiFS era. However, when Henson *et al.* (2010) compared historical trends in gyre area with several CORE-forced ocean biogeochemistry models (including the one used here), they found generally good agreement between modelled and observed gyre size (0.88 for the SeaWiFS era), but also found that the variability during the SeaWiFS era was much smaller than that required to detect an anthropogenic signal. Given the deficiencies of an Eulerian interpretation of ocean biome variability on short time-scales (Figure 7), as well as earlier results indicating that there are changes in the large-scale ventilation structure of the ocean under global warming (Gnanadesikan *et al.*, 2007), it will be essential not to depend on physical models alone to predict the behaviour of these biome boundaries.

Challenges in modelling high-latitude variability

We have demonstrated that interannual variation in the monthly distribution of productivity might be much larger than the interannual variation in annual mean productivity (Figure 4), and that at high latitudes, salinity can play an important role in explaining this variability (Figure 9). Variability in salinity presents a challenge to retrospective analyses of ecosystem variability. As demonstrated in Figure 4, the high-latitude variation in spring production is higher in ESM2.1 coupled climate models than in the CORE ocean-only reanalysis model. The main reason for this is that ocean-only models run with "observed" precipitation must be also run with a flux correction by which salinities are restored to their climatological values. Without such restoration, a chain of feedbacks may be triggered at high latitudes whereby cooling in convective regions results in precipitation exceeding evaporation, resulting in a build-up of freshwater at the surface, suppression of convection, and further cooling. In reality, a drop in surface temperatures would also be expected to result in a decrease in precipitation, but this feedback is absent in CORE-forced runs. However, restoration damps the interannual variability in salinity, especially when such variability is associated with large-scale advection of surface anomalies. The challenge then is for the climate community to develop methods of reanalysis that can properly simulate the variability in winds and heating without damping out hydrological feedbacks. Coupled reanalyses (Zhang *et al.*, 2007), where the atmospheric winds are nudged towards observed values, might provide such a consistent solution, but ecosystem models have yet to be included in such reanalyses. In the interim, fisheries oceanographers using CORE-forced runs should evaluate carefully whether observed salinity variability is properly captured.

Acknowledgments

Rob Armstrong and Jorge Sarmiento helped with the formulation of our original implementation of size structure within the models. Charlie Stock, Ryan Rykaczewski, and Vince Saba helped with understanding the implications and limitations of this approach and provided useful reviews of this manuscript. We thank Jon Hare for useful discussions and for the invitation to present this paper at the Sendai meeting, and to Shin-Ichi Ito and two anonymous reviewers for their comments on the manuscript.

References

Agawin, N. S. R., Duarte, C. M., and Agusti, S. 2000. Nutrient and temperature control of the contribution of picoplankton to phytoplankton biomass and production. Limnology and Oceanography, 45: 591–600.

Aita, M. N., Yamanaka, Y., and Kishi, M. J. 2003. Effect of ontogenetic vertical migration of zooplankton on the results of NEMURO embedded in a general circulation model. Fisheries Oceanography, 12: 284–290.

Aita, M. N., Yamanaka, Y., and Kishi, M. J. 2007. Interdecadal variation of the lower trophic ecosystem in the Northern Pacific between 1948 and 2002, in a 3-D implementation of the NEMURO model. Ecological Modelling, 202: 81–91.

Alvain, S., Moulin, C., Dandonneau, Y., and Loisel, H. 2008. Seasonal distribution and succession 10 of dominant phytoplankton groups in the global ocean: a satellite view. Global Biogeochemical Cycles, 22: GB3001. doi:10.1029/2007GB003154.

Aumont, O., and Bopp, L. 2006. Globalizing results from ocean *in situ* iron fertilization studies. Global Biogeochemical Cycles, 20: GB2017. doi:10.1029/2005GB002591.

Behrenfeld, M. J., Boss, E., Siegel, D. A., and Shea, D. M. 2005. Carbon-based ocean productivity and phytoplankton physiology from space. Global Biogeochemical Cycles, 19: GB1006. doi:10.1029/2004GB002299.

Bigelow, H. B. 1926. Plankton of the offshore waters of the Gulf of Maine. Bulletin of the US Bureau of Fisheries, 40. 509 pp.

Boulcott, P., and Wright, P. J. 2008. Critical timing for reproductive allocation in a capital breeder: evidence from sandeels. Aquatic Biology, 3: 31–40.

Carr, M-E. 2002. Estimation of potential productivity in eastern boundary currents using remote sensing. Deep Sea Research II, 49: 59–80.

Chavez, F. P., Ryan, J., Lluch-Costa, S. E., and Niquen, M. 2003. From anchovies to sardines and back, multidecadal change in the Pacific Ocean. Science, 299: 217–221.

Conkright, M. E., Locarnini, R. A., Garcia, H. E., O'Brien, T. D., Boyer, T. B., Stephens, C., and Antonov, J. I. 2002. World Ocean Atlas 2001: Objective Analysis, Data Statistics, and Figures. CD-ROM, National Oceanographic Data Center. Silver Spring, MD, USA.

Cushing, D. H. 1990. Plankton production and year-class strength in fish populations: an update of the match/mismatch hypothesis. Advances in Marine Biology, 26: 249–293.

De Boyer Montegut, C., Madec, G., Fischer, A. S., Lazar, A., and Iudicone, D. 2007. Mixed layer depth over the global ocean: an examination of profile data and a profile-based climatology, Journal of Geophysical Research, 109, C12003, doi:10.1029/2004JC002378.

Delworth, T. L., Broccoli, A. J., Rosati, A., Stouffer, R. J., Balaji, V., Beesley, J. A., Cooke, W., *et al.* 2006. GFDL's CM2 global coupled climate models: part 1—Formulation and simulation characteristics. Journal of Climate, 19: 643–674.

Dugdale, R. C., and Goering, J. J. 1967. Uptake of new and regenerated forms of nitrogen in primary productivity. Limnology and Oceanography, 12: 196–206.

Dunne, J. P., Armstrong, R. A., Gnanadesikan, A., and Sarmiento, J. L. 2005. Empirical and mechanistic models of the particle export ratio. Global Biogeochemical Cycles, 19: GB4026. doi:10.1029/2004GB002390.

Dunne, J. P., Gnanadesikan, A., Sarmiento, J. L., and Slater, R. D. 2010. Technical description of the prototype version (v0) of tracers of phytoplankton with allometric zooplankton (TOPAZ) ocean biogeochemical model as used in the Princeton IFMIP model. Biogeosciences, 7(Suppl.): 3593. http://www.biogeosciences.net/7/3593/2010/bg-7-3593-2010-supplement.pdf.

Follows, M., and Dutkewicz, S. 2002. Meteorological modulation of the North Atlantic spring bloom. Deep Sea Research II, 49: 321–344.

Frost, B. W., and Franzen, N. C. 1992. Grazing and iron limitation in the control of phytoplankton stock and nutrient concentration: a chemostat analogue of the Pacific equatorial upwelling zone. Marine Ecology Progress Series, 83: 291–303.

Galbraith, E. D., Gnanadesikan, A., Dunne, J. P., and Hiscock, M. R. 2010. Regional impacts of iron-light co-limitation in a global biogeochemical model. Biogeosciences, 7: 1043–1064.

Galbraith, E. D., Kwon, E. Y., Gnanadesikan, A., Rodgers, K. B., Griffies, S. M., Bianchi, D., and Sarmiento, J. L. Climate variability and radiocarbon in the CM2Mc earth system model. Journal of Climate. doi:10.1175/2011JCLI3919.1 In press.

Gargett, A. E. 1997. The optimal stability "window": a mechanism underlying decadal fluctuations in North Pacific salmon stocks? Fisheries Oceanography, 5: 109–117.

Geider, R. J., MacIntyre, H. L., and Kana, T. M. 1997. Dynamic model of phytoplankton growth and acclimation: response of the balanced growth rate and chlorophyll *a* to carbon ratio to light, nutrient limitation and temperature. Marine Ecology Progress Series, 148: 187–201.

Genner, M. J., Sims, D. W., Wearmouth, V. J., Southall, E. J., Southward, A. J., Henderson, P. A., and Hawkins, S. J. 2004. Regional climatic warming drives long-term community changes of British marine fish. Proceedings of the Royal Society of London, Series B–Biological Sciences, 271: 655–661.

Glynn, P. W., and de Weerdt, W. H. 1991. Elimination of two reef-building hydrocorals following the 1982–1983 *El Niño* warming event. Science, 253: 69–71.

Gnanadesikan, A., Dixon, K. W., Griffies, S. M., Balaji, V., Barreiro, M., Beesley, J. A., Cooke, W. F., *et al.* 2006. GFDL's CM2 global coupled climate models—Part 2: the baseline ocean simulation. Journal of Climate, 19: 675–697.

Gnanadesikan, A., Dunne, J. P., Key, R. M., Matsumoto, K., Sarmiento, J. L., Slater, R. D., and Swathi, P. S. 2004. Oceanic ventilation and biogeochemical cycling: understanding the physical mechanisms that produce realistic distributions of tracers and productivity. Global Biogeochemical Cycles, 18: GB4010. doi:10.1029/2003GB002097.

Gnanadesikan, A., Russell, J. L., and Zeng, F. 2007. How does ocean ventilation change under global warming? Ocean Science, 3: 43–53.

Griffies, S. M., Biastoch, A., Boning, C., Bryan, F., Danabasoglu, G., Chassignet, E. P., England, M. H., *et al.* 2009. Coordinated ocean-ice reference experiments (CORes). Ocean Modelling, 26: 1–46.

Griffies, S. M., Gnanadesikan, A., Dixon, K. W., Dunne, J. P., Gerdes, R., Harrison, M. J., Rosati, A., *et al.* 2005. Formulation of an ocean model for global climate simulations. Ocean Science, 1: 45–79.

Guénette, S., Heymans, S. J. J., Christensen, V., and Trites, A. W. 2006. Ecosystem models show combined effects of fishing, predation, competition and ocean productivity on Steller sea lions, (*Eumetopias jubatus*) in Alaska. Canadian Journal of Fisheries and Aquatic Sciences, 63: 2495–2517.

Hare, J. A., Alexander, M. A., Fogarty, M. J., Williams, E. H., and Scott, J. D. 2010. Forecasting the dynamics of a coastal fishery species using a coupled climate-population model. Ecological Applications, 20: 452–464.

Henson, S. A., Sarmiento, J. L., Dunne, J. P., Bopp, L., Lima, I., Doney, S. C., John, J., *et al.* 2010. Detection of anthropogenic climate change in satellite records of ocean chlorophyll and productivity. Biogeosciences, 7: 621–640.

Henson, S., and Thomas, A. 2007. Interannual variability in timing of bloom initiation in the California Current system. Journal of Geophysical Research: Oceans, 112: C08007. doi:10.1029/2006JC003960.

Hjort, J. 1914. Fluctuations in the great fisheries of northern Europe viewed in the light of biological research. Rapports et

Procès-Verbaux des Réunions du Conseil Permanent International pour l'Exploration de la Mer, 20: 1–228.

Hunt, G. L., Stabeno, P. J., Strom, S., and Napp, J. M. 2008. Patterns of spatial and temporal variation in the marine ecosystem of the southeastern Bering Sea. Deep Sea Research II, 55: 1919–1944.

Jonsson, K. I. 1997. Capital and income breeding as alternative tactics of resource use in reproduction. Oikos, 78: 57–66.

Kimura, S., and Tsukamoto, K. 2006. The salinity front in the North Equatorial Current: a landmark for the spawning migration of the Japanese eel (*Anguilla japonica*) related to the stock recruitment. Deep Sea Research II, 53: 315–325.

Kirby, D. S., Fiksen, O., and Hart, D. J. B. 2000. A dynamic optimisation model for the behaviour of tunas at ocean fronts. Fisheries Oceanography, 9: 328–342.

Kishi, M. J., Kaeriyama, M., Ueno, H., and Kamezawa, Y. 2010. The effect of climate change on the growth of Japanese chum salmon (*Oncorhynchus keta*) using a bioenergetics model coupled with a three-dimensional lower tropic ecosystem model (NEMURO). Deep Sea Research II, 57: 1257–1265.

Klausmeier, C., Litchman, E., Daufresne, T., and Levin, S. A. 2004. Optimal nitrogen-to-phosphorus stoichiometry of phytoplankton. Nature, 429: 171–174.

Kostadinov, T. S., Siegel, D. A., and Maritorena, S. 2009. Retrieval of the particle size distribution from satellite ocean color observations. Journal of Geophysical Research: Oceans, 114: C09015. doi:10.1029/2009JC005303.

Mantua, N. R., Hare, S. R., Zhang, Y., Wallace, J. M., and Francis, R. C. 1997. A Pacific interdecadal climate oscillation with impacts on salmon production. Bulletin of the American Meteorological Society, 78: 1069–1079.

Martin, K., and Wiebe, K. L. 2004. Coping mechanisms of alpine and Arctic breeding birds: extreme weather and limitations to reproductive resilience. Integrative and Comparative Biology, 44: 177–185.

Martinez, E., Antoine, D., D'Ortenzio, F., and Gentili, B. 2009. Climate-driven basin-scale decadal oscillations of oceanic phytoplankton. Science, 326: 1253–1256.

Moore, J. K., Doney, S. C., Kleypas, J. A., Glover, D. M., and Fung, I. Y. 2002. An intermediate complexity marine ecosystem model for the global domain. Deep Sea Research II, 49: 463–507.

Mouw, C. B., and Yoder, J. A. 2010. Optical determination of phytoplankton size composition from global SeaWiFS imagery. Journal of Geophysical Research: Oceans, 115: C12018. doi:10.1029/2010JC006637.

Piroddi, C., Giovanni, B., and Christensen, V. 2010. Effects of local fisheries and ocean productivity on the northeastern Ionian Sea ecosystem. Ecological Modelling, 221: 1526–1544.

Platt, T., Subba Rao, D. V., and Irwin, B. 1983. Photosynthesis of picoplankton in the oligotrophic ocean. Nature, 301: 702–704.

Polovina, J. J., Dunne, J. P., Woodworth, P. A., and Howell, E. A. 2011. Projected expansion of the subtropical biome and contraction of the temperate and equatorial upwelling biomes in the North Pacific under global warming. ICES Journal of Marine Science, 68: 986–995.

Polovina, J. J., Howell, E. A., and Abecassis, M. 2008. Ocean's least productive waters are expanding. Geophysical Research Letters, 35: L03618. doi:10.1029/2007GL031745.

Reichler, T., and Kim, J. 2008. How well do coupled climate models simulate today's climate? Bulletin of the American Meteorological Society, 89: 303–311.

Russell, J. L., Stouffer, R. J., and Dixon, K. W. 2006. Intercomparison of the Southern Ocean circulations in IPCC coupled model control simulations. Journal of Climate, 19: 4560–4575.

Ryther, J. H. 1969. Photosynthesis and fish production in the sea. Science, 166: 72–76.

Sarmiento, J. L., Slater, R., Bopp, L., Doney, S. C., Hirst, A. C., Kleypas, J., Matear, R. J., *et al.* 2004. Response of ocean ecosystems to climate warming. Global Biogeochemical Cycles, 18: GB3003. doi:10.1029/2003GB002134.

Sarmiento, J. L., Slater, R. D., Dunne, J. P., Gnanadesikan, A., and Hiscock, M. R. 2010. Small-scale carbon mitigation by patch iron fertilization. Biogeosciences, 7: 3593–3636.

Schneider, B., Bopp, L., Gehlen, M., Segschneider, J., Frolicher, T. L., Cadule, P., Friedlingstein, P., *et al.* 2008. Climate-induced interannual variability of marine primary and export production in three global coupled carbon cycle models. Biogeosciences, 5: 597–614.

Six, K. D., and Meier-Reimer, E. 1996. Effects of plankton dynamics on seasonal carbon fluxes in an ocean general circulation model. Global Biogeochemical Cycles, 10: 559–583.

Steinacher, M., Joos, F., Frohlicher, T. L., Bopp, L., Cadule, P., Cocco, V., Doney, S. C., *et al.* 2010. Projected 21st century decrease in marine productivity: a multi-model analysis. Biogeosciences, 7: 979–1005.

Sugimoto, T., Kimura, S., and Tadokoro, K. 2001. Impact of *El Niño* events and climate regime shift on living resources in the western North Pacific. Progress in Oceanography, 49: 113–127.

Uitz, J., Claustre, H., Gentili, B., and Stramski, D. 2010. Phytoplankton class-specific primary production in the world's oceans: Seasonal and interannual variability from satellite observations. Global Biogeochemical Cycles, 24: GB3016. doi:10.1029/2009GB003680.

Van Oldenborgh, G. J., Philip, S. Y., and Collins, M. 2005. *El Niño* in a changing climate: a multi-model study. Ocean Science, 1: 81–95.

Wittenberg, A. T., Rosati, A., Lau, N. G., and Ploshay, J. J. 2006. GFDL's CM2 global coupled climate models, part III: tropical Pacific climate and ENSO. Journal of Climate, 19: 698–722.

Zhang, S., Harrison, M. J., Rosati, A., and Wittenberg, A. T. 2007. System design and evaluation of coupled ensemble data assimilation for global oceanic climate studies. Monthly Weather Review, 135: 3541–3564.